Evolution of Pyrrhae Fossae, Mars: an explication from the age estimation using the Buffered Crater Counting technique

Keyur De[1,2,*], Trishit Ruj[3], Abhik Kundu[2], Nilanjan Dasgupta[1] and Kenji Kawai[4]

[1]Department of Geology, Presidency University, 86/1 College Street, Kolkata 700 073, India
[2]Department of Geology, Asutosh College, 92, S.P. Mukherjee Road, Kolkata 700 026, India
[3]Institute of Space and Astronautical Science, Japan Aerospace Exploration Agency, Kanagawa 252-5210, Japan
[4]Department of Earth and Planetary Science, School of Science, University of Tokyo, Hongo 7-3-1, Bunkyo, Tokyo 113-0033, Japan

Pyrrhae Fossae (PyFo) on Mars is a palaeo-extensional tectonic feature preserved within a Noachian basement in the north-western Noachis Terra (NT). We have tried to understand the possible origin of the stress responsible for the evolution of these tectonic structures and to correlate their formation with other global Martian events. We estimated the absolute model age of PyFo, using the Buffered Crater Counting (BCC) technique, which indicates that these extensional structures were formed at ~3.79 Ga, after the basement formation at ~3.98 Ga. Considering the ages and geology of the terrains adjoining the PyFo region, we propose that the regional scale flexural bending was promoted either in response to Tharsis-related volcano-tectonic load or thinning of northern lowlands producing extension at the upper crustal level, generating these fossae at the early stage of Martian evolution.

Keywords: Buffered Crater Counting, extension, flexure, Noachis Terra, Pyrrhae Fossae.

MARS was dynamically active, at the very early stage of its evolution[1], driven by its internal heat transfer from the interior to the surface. Tectonic activities peaked during the Noachian time and continued later with much-decreased intensity concentrating around certain domains[2,3], long after the cessation of the Martian internal core dynamo (~4 Ga (refs 4, 5); alternatively ~3.7 Ga (ref. 6)). Even the recent InSight mission found the planet seismically active and detected seismic response similar to terrestrial intraplate[7]. However, the absence of intense surface reconstruction (apart from some volcanic domains[8] combined with a significantly low rate of erosion[9,10]) led to the preservation of the early tectonic signatures, especially in the southern highlands of Mars. The Noachis Terra (NT), part of the southern highlands, preserves early tectonic signatures of both tensional and compressional regimes. Large (up to 1000 km in length) grabens of late Noachian age are present in the eastern part of the NT, adjacent to the Hellas Basin[11,12], while comparatively smaller grabens (~20–120 km long) are found[13,14] in the north-western part of the NT. One such set of narrow grabens (termed as fossae) trending E–W is the Pyrrhae Fossae (PyFo, Figure 1). The PyFo drew our attention for its unique morphology and structural orientation, which is different from the nearby tensional structures, especially grabens (grabens surrounding PyFo are WNW–ESE, NE–SW, N–S in orientation). All the grabens to the west of the PyFo are parts of the radial graben system related to the Tharsis, the giant volcano–tectonic province. The detailed morpho-structural analysis of PyFo has been explained in our previous study[15]. However, their origin, evolution, and relationship with the global Martian tectonic events remained elusive. To understand the origin and evolution, knowledge of the timing of the formation of these grabens is essential. Therefore, we have estimated the absolute age of the PyFo using the BCC technique and discussed their evolution and possible origin.

Pyrrhae Fossae

PyFo and its surrounding region located to the NE of the Argyre basin (Figure 1) are confined within the middle Noachian highland units[16]. The extracted Mars Orbiter Laser Altimeter (MOLA) Digital Elevation Model (DEM)[17] reveals that the elevation of the PyFo and its surrounding region varies from –3 to +2 km (with respect to the zero-elevation level) and shows a general slope (Figure 2) towards the northern lowlands. Constant E–W orientation of these fossae was observed to appear over an area of ~150,000 sq. km. Lengths and widths of individual fossa vary from 20 to 120 km and 6 to 13 km respectively. The floors of individual fossae show a dropdown (vertical component) of ~20–~325 m from the adjacent ground level. The northernmost fossae of PyFo has deformed an unnamed crater (centred at 23.1°W, 27.5°S), which facilitated the identification of the nature

*For correspondence. (e-mail: de.keyur@gmail.com)

of the grabens. Though the crater rim is faint in the north-eastern part due to prolonged weathering and erosion (wind streaks and channels present in and around the crater[15] indicate wind and water activity in the region), the rim remained almost circular with no visible offset along the faults bounding the fossae, suggesting that the normal faults bordering the fossae are dip–slip in nature[15]. Considering the nature of the fault planes bounding the fossae, De *et al.*[15] analysed the orientation of palaeostress responsible for their formation, which revealed that N–S trending sub-horizontal maximum tensile stress (σ_3) and sub-vertical maximum compressive stress (σ_1) resulted in the formation of the PyFo.

Dataset and software

Identification of the fault-scarps of the normal faults bounding the PyFo was executed using MOLA DEM[17] (resolution: 463 m/pixel) and Thermal Emission Imaging System-Infrared (THEMIS-IR) Day Global Mosaic[18] (resolution: 100 m/pixel) images. High-Resolution Stereo Camera[19,20] (HRSC) (resolution: 12.5 to 50 m/pixel) and Context Camera[21] (CTX) images (resolution: 6 m/pixel) were used to identify and distinguish the stratigraphic relations of the crater ejecta blankets. Geological mapping of the area and crater counting were performed on HRSC and CTX images using the CraterTools[22] add-on in the Arc-GIS. Extracted crater statistics were then analysed in Craterstats[23] (version: 2.0) to estimate the age.

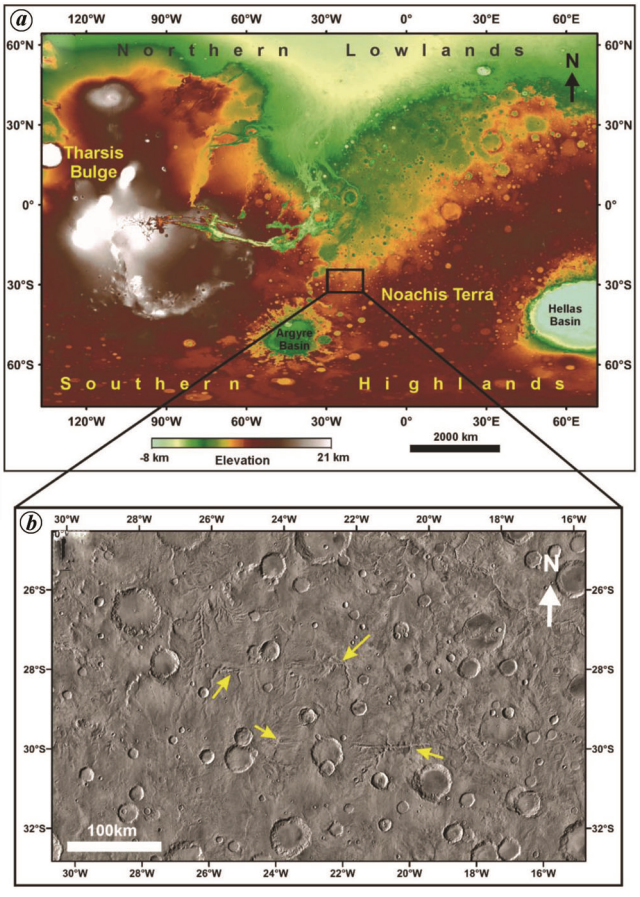

Figure 1. ***a***, MOLA DEM showing the location of the PyFo (marked with a black rectangle) in the NT. ***b***, THEMIS-IR Day Global Mosaic showing area of study. Individual fossae of the PyFo considered for the BCC analysis are marked with yellow arrows.

Age estimation methodology

Determination of absolute model ages of the planetary surfaces by analysing crater size-frequency distributions (CSFDs) is the common technique to estimate ages of planetary surfaces[24–28]. In this technique, all the superimposed craters with centres inside the boundary (of a geologically homogeneous area) are counted. The CSFDs obtained by crater counting is then fitted with a known crater production function (PF)[23]. To obtain the absolute age, the crater frequencies for certain crater sizes are then combined with chronology function (CF)[29]. However, linear/curvilinear features are more susceptible to the resurfacing processes, including aqueous alteration, and wind-driven erosion erasing the original crater population[30]. Therefore, the traditional CSFD technique cannot extract reliable surface ages as it requires the number of craters normalized to the mapped area, which is very limited for linear/curvilinear features resulting in poor crater statistics[30].

BCC

The BCC method (previously called 'crater line-count method[31]') allows us to determine the age of linear/curvilinear structures individually, regardless of the surrounding geological unit or resurfacing processes within the counting area. In BCC[30,32], crater statistics are

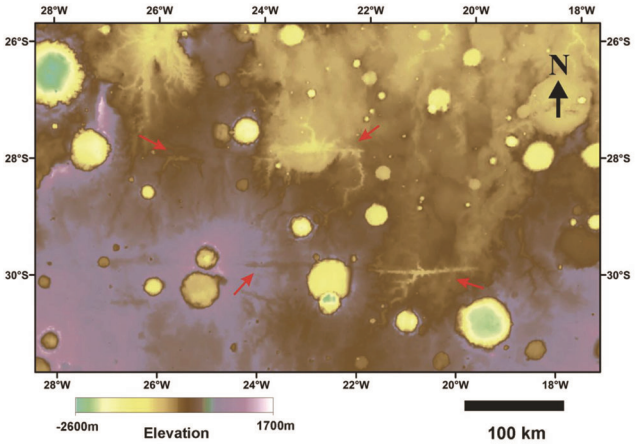

Figure 2. MOLA DEM showing the topography of PyFo region. Individual fossae of the PyFo considered for the BCC analysis are shown with red arrows.

improved by considering a buffer area around the linear/curvilinear feature in the analysis of CSFDs.

Unlike the traditional CSFD analysis, the BCC technique considers every superimposed crater, postdating the structures, irrespective of the location of their centres or sizes[30,32]. Crater ejecta is also considered while determining the buffer to incorporate more craters to improve the crater statistics (called ejecta approach in particular). The effective counting area (which includes a buffer around the linear/curvilinear feature) for the analysis of CSFDs is determined for each postdating crater; depending upon the buffer width, the effective crater frequency is then calculated individually for each crater. The calculated buffer around the linear/curvilinear feature depends on the diameter of the counted crater[30]. After several modifications, this technique has recently been applied to several varied linear/curvilinear features (tectonic structures[12,33–38], fluvial features[32], and impact-related features[39–41]).

Age estimation methodology of PyFo

Linear scarp walls of PyFo are very narrow and may have suffered resurfacing processes. Therefore, to obtain the age with more precision, we have applied the BCC technique. The scarp walls of the PyFo were mapped as elongated polygons (Figure 3). We excluded the fossae floors from mapping and craters present on these floors from counting as they may pre-date the fossae. Secondary craters, crater clusters and crater-like circular depressions such as volcanic calderas, collapse, and sublimation pits were also carefully omitted while counting. Craters with or without their ejecta blankets superposed on the walls of fossae were considered, following the principles of BCC[30,32]. Craters were mapped using a three-point crater digitizing tool (CraterTools). The buffer area was autogenerated by CraterTools around the boundary of the fossae, considering the three crater radii buffer (the ejecta approach). Upon completion, crater statistics were exported to a special crater count (SCC) file for analysing the CSFDs in Craterstats. The PF of Ivanov[42] and the CF of Hartmann and Neukum[27] were used to derive the absolute model ages along with the epoch boundaries specified by Werner and Tanaka[43] and subsequently modified by Michael[44].

We have also determined the age of the geological unit in which the fossae are present locally by analysing the CSFDs. The boundary of the measurement area was selected with the help of the geological map of Mars[16] to ensure the homogeneity of the surface. Craters with their centres located well inside the mapped boundary (following conventional CSFD method) (Figure 4) were considered to estimate the age of the basement geological unit into which the fossae were emplaced.

Results and discussion

We found that the age of PyFo is $3.79^{+0.058}_{-0.097}$ Ga by analysing craters in a diameter range of 6–50 km (Figure 5). The estimated age of the basement geological unit of the region is $3.98^{+0.038}_{-0.052}$ Ga (Figure 6). These results indicate that the PyFo formed in late Noachian time (~3.86–3.74 Ga (refs 42, 43)), shortly after the formation of the basement in early Noachian time (~3.99–3.97 Ga (refs 43, 45)). Our study also indicates that the basement unit is formed earlier (early Noachian) than the previously estimated time (middle Noachian[16]).

The orientations of PyFo do not follow the outer arc curvature of the major impact basins (e.g. Argyre of ~3.83 Ga (ref. 45); Holden of ~3.5 Ga (ref. 46); Ladon of

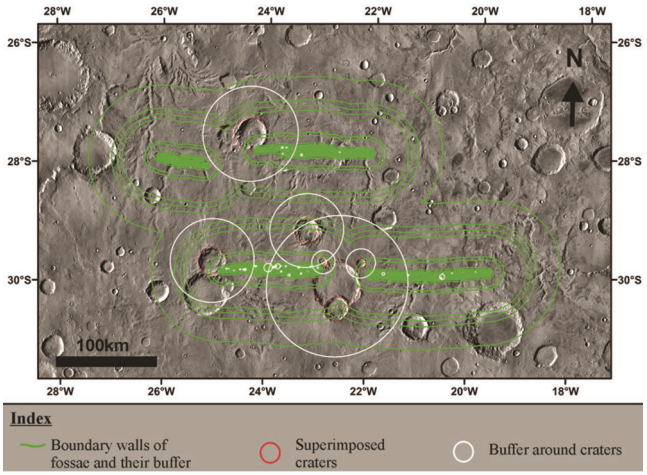

Figure 3. THEMIS-IR Day Global Mosaic of the PyFo showing faulted boundary walls of fossae and superimposed craters mapped in the green polygon and red outline respectively. Buffers around craters (3 radii) and faulted boundary walls are marked in white and green outline respectively.

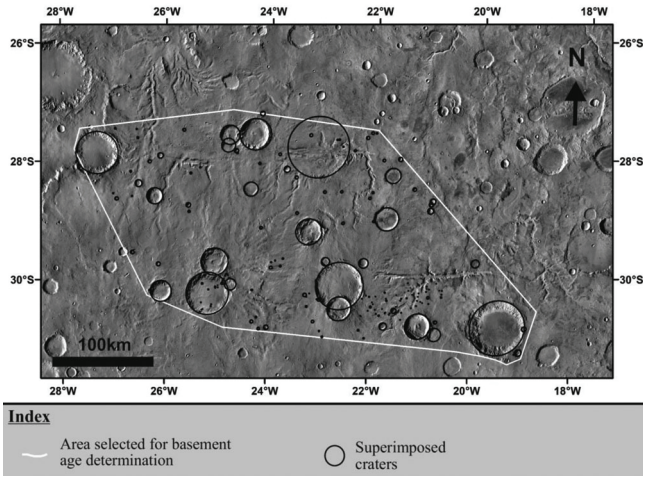

Figure 4. THEMIS-IR Day Global Mosaic showing area selected for determinating the age of the basement and the craters counted in the PyFo region are marked in white and black outline respectively.

~4.0 Ga (ref. 47)), situated in its vicinity (within 1000 km). Note that large impacts tend to form radial and concentric fractures around them. Due to the evolution of the underlying mantle through time, isostatic adjustment leads to movement of the upper lithosphere to the basin centre[11] developing concentric faults around them. However, extensional structures in the west of the PyFo are dominantly WNW–ESE in orientation and are related to the development of the Tharsis and its components. Grabens present on the south of PyFo significantly contrast in orientation (N–S) and are broadly concentric to the Argyre basin. Structures related to the Hellas basin (~3.99 Ga (ref. 45)) present ~3000 km east of these fossae, are mostly wider (~100 km) and have NE–SW trend[48].

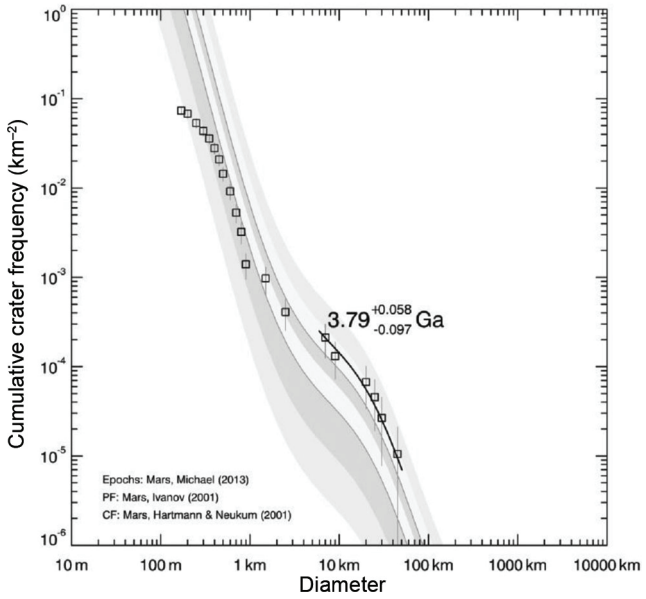

Figure 5. The CSFDs and derived model ages of the PyFo (marked in Figure 3) using the BCC technique.

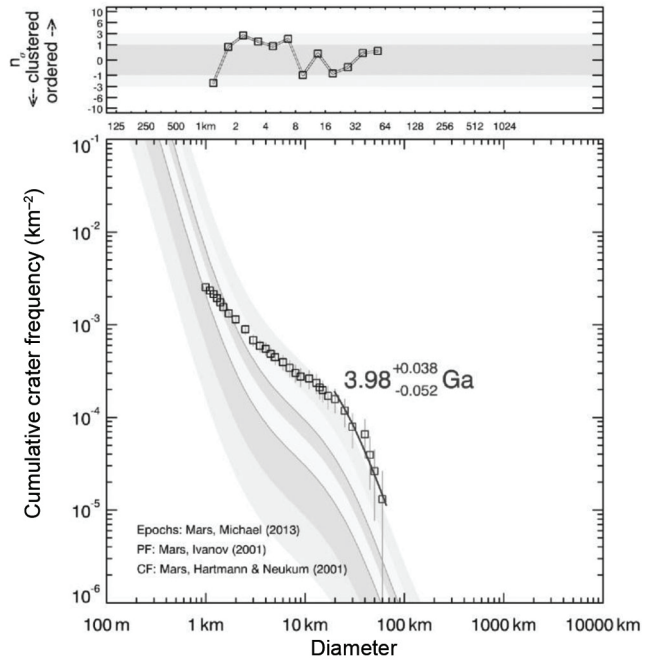

Figure 6. The CSFDs and derived model ages of the basement (area marked in Figure 4) of PyFo.

These age and orientation differences suggest that the extensional event that formed the PyFo is not related to any of these major events.

Most of the extensional tectonic structures in the western hemisphere of Mars are proposed to be related to the development of the Tharsis volcano-tectonic province and formed before 3.8 Ga (ref. 49). Grabens present to the west of the PyFo are radial to the Tharsis and possibly formed during early-middle Noachian time when Tharsis volcano-tectonic activity was centred at the Claritas region[2,50]. However, the present study shows that the PyFo formed in the late Noachian time, much later than the development of Tharsis radial grabens of the surrounding region. Moreover, PyFo also differs in orientation from the Tharsis-related grabens. These together indicate that the evolution of Tharsis has no direct bearing on the formation of PyFo, and possibly a different tectonic event was responsible for its formation.

Elastic spherical shell loading model[51–55] successfully explains the present-day geoid assuming Tharsis as a massive load supported by membrane stresses in a rigid lithosphere. The surface of Mars outside the Tharsis behaves as a thin spherical deformed lithospheric membrane[55]. Formation of the PyFo can be related to the deformation of this elastic membrane by the phenomenon of membrane[55] tectonics, which plays a key role in crustal-scale deformation at an early stage of planetary evolution. The huge volcanic load of Tharsis might have produced layer parallel differential stresses developed due to isostatic adjustment at a later stage, within this thin crust which bent to accommodate the sub-horizontal differential stress field. Such stress-induced regional-scale flexural bending of the lithosphere might have led to the fractures at the upper crustal levels at late Noachian time (Figure 7). These fractures may show parallelism in their strike but vary in length, spaced out over an area of hundreds of kilometres.

Alternatively, these flexure-induced extensional fractures in the comparatively thicker crust of southern highlands might have resulted from thinning of northern lowlands. Watters[56] envisaged lithospheric flexure in the southern highlands of Mars due to the thinning of northern lowland crust from a study in the eastern hemisphere. It is also possible that thinning of northern lowlands in the western hemisphere induced flexural bending of the lithosphere beneath the southern highlands and resulted in the extension of the uppermost crust, ultimately producing the PyFo.

Therefore, we propose that in the late Noachian time flexural bending of the lithosphere induced either by

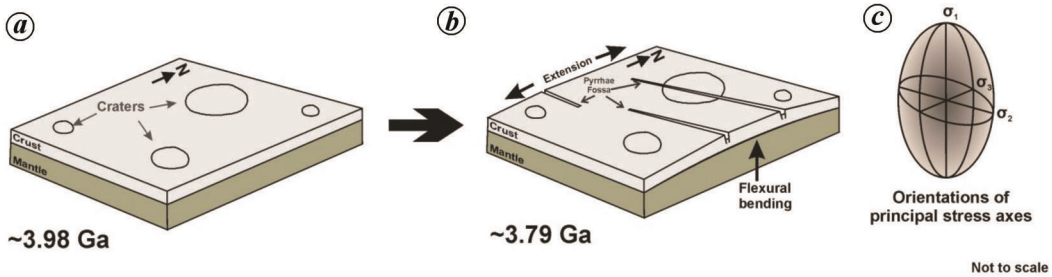

Figure 7. Schematic illustration of the formation of PyFo by the flexural bending of the crust. ***a***, Before the formation of the PyFo; ***b***, After the formation of PyFo; ***c***, Orientations of principal stress axes (σ_1: maximum, σ_2: intermediate, σ_3: minimum) responsible for the development of the normal faults bounding PyFo.

loading of Tharsis or by thinning of northern lowlands produced fractures in the upper crust leading to an extensional regime producing normal faults, bounding the PyFo.

1. Baker, V. R., Maruyama, S. and Dohm J. M., Tharsis superplume and the geological evolution of early Mars. In *Superplumes: Beyond Plate Tectonics* (eds Yuen, D. A. *et al.*), Springer, 2007, pp. 507–522.
2. Anderson, R. C. *et al*., Primary centers and secondary concentrations of tectonic activity through time in the western hemisphere of Mars. *J. Geophys. Res. E Planets*, 2001, **106**(E9), 20563–20585.
3. Anderson, R. C., Dohm, J. M., Haldemann, A. F. C., Pounders, E., Golombek, M. and Castano, A., Centers of tectonic activity in the eastern hemisphere of Mars. *Icarus*, 2008, **195**(2), 537–546.
4. Acuña, M. H. *et al.*, Global distribution of crustal magnetization discovered by the Mars Global Surveyor MAG/ER experiment. *Science*, 1999, **284**(5415), 790–793.
5. Connerney, J. E. P. P. *et al.*, Tectonic implications of Mars crustal magnetism. *Proc. Natl. Acad. Sci.*, 2005, **102**(42), 14970–14975.
6. Mittelholz, A., Johnson, C. L., Feinberg, J. M., Langlais, B. and Phillips, R. J., Timing of the martian dynamo: New constraints for a core field 4.5 and 3.7 Ga ago. *Sci. Adv.*, 2020, **6**(18), 0513.
7. Banerdt, W. B. *et al.*, Initial results from the InSight mission on Mars. *Nat. Geosci.*, 2020, **13**, 183–189.
8. Werner, S. C., The global martian volcanic evolutionary history. *Icurus*, 2009, **201**(1), 44–68.
9. Golombek, M. P. and Bridges, N. T., Erosion rates on Mars and implications for climate change: constraints from the Pathfinder landing site. *J. Geophys. Res.*, 2000, **105**(E1), 1841–1853.
10. Carr, M. H. and Head III, J. W., Geologic history of Mars. *Earth Planet. Sci. Lett.*, 2010, **294**, 185–203.
11. Wichman, R. W. and Schultz, P. H., Sequence and mechanisms of deformation around the Hellas and Isidis Impact Basins on Mars. *J. Geophys. Res.*, 1989, **94**(B12), 17333.
12. Ruj, T., Komatsu, G., Pasckert, J. H. and Dohm, J. M., Timings of early crustal activity in southern highlands of Mars: periods of crustal stretching and shortening. *Geosci. Front.*, 2019, **10**(3), 1029–1037.
13. De, K., Kundu, A., Dasgupta, N. and Kawai, K., Establishing the control of pre-existing tectonic structures on the channel courses by orientation analyses: a case study from Noachis Terra and Margaritifer Terra, Mars. In Lunar Planet. Science Conference, 2020, p. 1932.
14. De, K., Dasgupta, N. and Kundu, A., A statistical approach to decipher the tectonic control on the geometry of Martian channels: case study from Pyrrhae Fossae, Noachis Terra, Mars. *Planet. Space Sci.*, 2018, **164**, 174–183.
15. De, K., Kundu, A., Chauhan, P. and Dasgupta, N., An example of consistent palaeostress regime resulting in morphometric irregularity in the northwestern part of Noachis Terra, Mars. *Curr. Sci.*, 2015, **108**(12), 2156–2159.
16. Tanaka, K. L., Robbins, S. J., Fortezzo, C. M., Skinner, J. A. and Hare, T. M., The digital global geologic map of Mars: chronostratigraphic ages, topographic and crater morphologic characteristics, and updated resurfacing history. *Planet. Space Sci.*, 2014, **95**, 11–24.
17. Smith, D. E. *et al.*, Mars Orbiter Laser Altimeter: experiment summary after the first year of global mapping of Mars. *J. Geophys. Res. E Planets*, 2001, **106**(E10), 23689–23722.
18. Christensen, P. R. *et al.*, The thermal emission imaging system (THEMIS) for the Mars 2001 Odyssey Mission. *Space Sci. Rev.*, 2004, **110**, 85–130.
19. Jaumann, R. *et al.*, The high-resolution stereo camera (HRSC) experiment on Mars express: instrument aspects and experiment conduct from interplanetary cruise through the nominal mission. *Planet. Space Sci.*, 2007, **55**, 928–952.
20. Neukum, G. and Jaumann, R., HRSC: the high resolution stereo camera of Mars express. *Eur. Sp. Agency, Special Publ. ESA SP*, 2004, **1240**, 17–35.
21. Malin, M. C. *et al.*, Context camera investigation on board the Mars reconnaissance orbiter. *J. Geophys. Res.*, 2007, **112**(E5), E05S04.
22. Kneissl, T., Van Gasselt, S. and Neukum, G., Map-projection-independent crater size-frequency determination in GIS environments – new software tool for ArcGIS. *Planet. Space Sci.*, 2011, **59**, 1243–1254.
23. Michael, G. G. and Neukum, G., Planetary surface dating from crater size-frequency distribution measurements: Partial resurfacing events and statistical age uncertainty. *Earth Planet. Sci. Lett.*, 2010, **294**, 223–229.
24. Hartmann, W. K., Martian Cratering. *Icarus*, 1966, **5**, 565–576.
25. Hartmann, W. K., Martian cratering III: theory of crater obliteration. *Icarus*, 1971, **15**(3), 410–428.
26. Neukum, G. and Wise, D. U., Mars: a standard crater curve and possible new time scale. *Science*, 1976, **194**(4272), 1381–1387.
27. Hartmann, W. K. and Neukum, G., Cratering chronology and the evolution of Mars. *Space Sci. Rev.*, 2001, **96**, 165–194.
28. Neukum, G. *et al.*, The geologic evolution of Mars: episodicity of resurfacing events and ages from cratering analysis of image data and correlation with radiometric ages of Martian meteorites. *Earth Planet. Sci. Lett.*, 2010, **294**, 204–222.
29. Fassett, C. I., Analysis of impact crater populations and the geochronology of planetary surfaces in the inner solar system. *J. Geophys. Res. E Planets*, 2016, **121**(10), 1900–1926.
30. Kneissl, T., Michael, G. G., Platz, T. and Walter, S. H. G., Age determination of linear surface features using the Buffered Crater Counting approach – case studies of the Sirenum and Fortuna Fossae graben systems on Mars. *Icarus*, 2015, **250**, 384–394.

31. Tanaka, K. L., A new time-saving crater-count technique, with application to narrow features. In *NASA Technical Memo*, NASA, 1982, p. TM-85127.
32. Fassett, C. I. and Head, J. W., The timing of martian valley network activity: constraints from buffered crater counting. *Icarus*, 2008, **195**(1), 61–89.
33. Basilevsky, A. T., Head, J. W., Fassett, C. I. and Michael, G., History of tectonic deformation in the interior plains of the Caloris basin, mercury. *Sol. Syst. Res.*, 2011, **45**, 471–497.
34. Fegan, E. R., Rothery, D. A., Conway, S. J., Anand, M. and Massironi, M., Linking the timing of volcanic and tectonic features on Mercury: results from buffered crater counting. In European Planetary Science Congress, 2014, pp. EPSC2014–444.
35. Giacomini, L., Massironi, M., Marchi, S., Fassett, C. I., Di Achille, G. and Cremonese, G., Age dating of an extensive thrust system on mercury: implications for the planet's thermal evolution. *Geol. Soc. Spec. Publ.*, 2015, **401**, 291–311.
36. Ruj, T., Komatsu, G., Pondrelli, M., Di Pietro, I. and Pozzobon, R., Morphometric analysis of a Hesperian aged Martian lobate scarp using high-resolution data. *J. Struct. Geol.*, 2018, **113**, 1–9.
37. Yue, Z., Michael, G. G., Di, K. and Liu, J., Global survey of lunar wrinkle ridge formation times. *Earth Planet. Sci. Lett.*, 2017, **477**, 14–20.
38. Ruj, T. and Kawai, K., A global investigation of wrinkle ridge formation events; implications towards the thermal evolution of Mars. *Icarus*, 2021, **369**, 114625.
39. Fassett, C. I. *et al.*, Caloris impact basin: exterior geomorphology, stratigraphy, morphometry, radial sculpture, and smooth plains deposits. *Earth Planet. Sci. Lett.*, 2009, **285**, 297–308.
40. Fassett, C. I. *et al.*, Lunar impact basins: stratigraphy, sequence and ages from superposed impact crater populations measured from Lunar Orbiter Laser Altimeter (LOLA) data. *J. Geophys. Res. E Planets*, 2012, **117**(E12), E00H06.
41. Bamberg, M., Jaumann, R., Asche, H., Kneissl, T. and Michael, G. G., Floor-fractured craters on mars – observations and origin. *Planet. Space Sci.*, 2014, **98**, 146–162.
42. Ivanov, B. A., Mars/Moon cratering rate ratio estimates. *Space Sci. Rev.*, 2001, **96**, 87–104.
43. Werner, S. C. and Tanaka, K. L., Redefinition of the crater-density and absolute-age boundaries for the chronostratigraphic system of Mars. *Icarus*, 2011, **215**(2), 603–607.
44. Michael, G. G., Planetary surface dating from crater size-frequency distribution measurements: multiple resurfacing episodes and differential isochron fitting. *Icarus*, 2013, **226**(1), 885–890.
45. Werner, S. C., The early martian evolution – constraints from basin formation ages. *Icarus*, 2008, **195**(1), 45–60.
46. Mangold, N. *et al.*, The origin and timing of fluvial activity at Eberswalde crater, Mars. *Icarus*, 2012, **220**(2), 530–551.
47. Robbins, S. J., Hynek, B. M., Lillis, R. J. and Bottke, W. F., Large impact crater histories of Mars: the effect of different model crater age techniques. *Icarus*, 2013, **225**(1), 173–184.
48. Ruj, T., Komatsu, G., Dohm, J. M., Miyamoto, H. and Salese, F., Generic identification and classification of morphostructures in the Noachis-Sabaea region, southern highlands of Mars. *J. Maps*, 2017, **13**(2), 755–766.
49. Golombek, M. P. and Phillips, R. J., Mars tectonics. In *Planetary Tectonics* (eds Watters, T. R. and Schultz, R. A.), Cambridge University Press, 2010, pp. 183–232.
50. Bouley, S., Baratoux, D., Paulien, N., Missenard, Y. and Saint-Bézar, B., The revised tectonic history of Tharsis. *Earth Planet. Sci. Lett.*, 2018, **488**, 126–133.
51. Banerdt, W. B., Phillips, R. J., Sleep, N. H. and Saunders, R. S., Thick shell tectonics on one-plate planets: applications to Mars. *J. Geophys. Res.*, 1982, **87**(B12), 9723–9733.
52. Banerdt, W. B., Golombek, M. P. and Tanaka, K. L., Stress and tectonics on Mars. In *Mars* (eds Kieffer, H. H. *et al.*), University of Ariz Press, Tucson, 1992, pp. 249–297.
53. Dimitrova, L. L., Holt, W. E., Haines, A. J. and Schultz, R. A., Toward understanding the history and mechanisms of Martian faulting: The contribution of gravitational potential energy. *Geophys. Res. Lett.*, 2006, **33**(8), L08202.
54. Phillips, R. J. *et al.*, Ancient geodynamics and global-scale hydrology on Mars. *Science*, 2001, **291**(5513), 2587–2591.
55. Phillips, R. J., Johnson, C. L. and Dombard, A. J., Localized Tharsis loading on Mars: testing the membrane surface hypothesis. In 35th Lunar and Planetary Science Conference, Houston, 2004, p. 1427.
56. Watters, T. R., Lithospheric flexure and the origin of the dichotomy boundary on Mars. *Geology*, 2003, **31**(3), 271–274.

ACKNOWLEDGEMENTS. K.D., A.K. and N.D. acknowledge support from the Space Applications Centre, ISRO Grant document no. D0798486 (11 February 2014). T.R. and K.K. acknowledge support from JSPS KAKENHI Grant Number 18F18312.

Received 20 August 2020; revised accepted 24 August 2021

doi: 10.18520/cs/v121/i7/906-911